Nanoscale

PAPER

View Article Online
View Journal

Cite this: DOI: 10.1039/c5nr01151e

Manipulating the glass transition behavior of sulfonated polystyrene by functionalized nanoparticle inclusion†

Sung-Kon Kim,‡[a] Ngoc A. Nguyen,‡[b] Jeong Jae Wie*§[c] and Ho Seok Park*[d]

Received 17th February 2015,
Accepted 10th April 2015

DOI: 10.1039/c5nr01151e

www.rsc.org/nanoscale

Nanoscale interfaces can modify the phase transition behaviors of polymeric materials. Here, we report the double glass transition temperature (T_g) behavior of sulfonated polystyrene (sPS) by the inclusion of 14 nm amine-functionalized silica (NH_2–SiO_2) nanoparticles, which is different from the single T_g behaviors of neat sPS and silica (SiO_2)-filled sPS. The inclusion of 20 wt% NH_2–SiO_2 nanoparticles results in an increase of T_g by 9.3 °C as well as revealing a second T_g reduced by 44.7 °C compared to the T_g of neat sPS. By contrast, when SiO_2 nanoparticles with an identical concentration and size to NH_2–SiO_2 are dispersed, sPS composites possess a single T_g of 7.3 °C higher than that of the neat sPS. While a nanoscale dispersion is observed for SiO_2 nanoparticles, as confirmed by microscopic and X-ray scattering analyses, NH_2–SiO_2 nanoparticles show the coexistence of micron-scale clustering along with a nanoscale dispersion of the individual nanoparticles. The micro-phase separation contributes to the free volume induced T_g reduction by the plasticization effect, whereas the T_g increase originates from the polymer segment mobility constrained by nanoconfinement and the rigid amorphous fractions deriving from strong polymer–particle interactions.

Introduction

Nanoscale confinement effects on polymer glass transition have recently drawn great attention for their dramatic deviation from bulk properties and have been investigated in the geometry of thin films[1,2] and nanoparticle-filled structured polymer composites.[3–5] Several studies have been conducted to bridge the non-classical phenomena observed from these two geometries.[6,7] An anomalous glass transition temperature change of a thin film is considered a free surface effect at the nanoscale and also strongly correlated to polymer–substrate interactions[8–10] and film thickness.[10–13] Nanoconfinement in thin film geometry has been extensively studied with various techniques, including ellipsometry,[14,15] capacitive dilatometry,[16] fluorescence,[2] neutron scattering reflectivity[17] and inelastic neutron scattering.[18] For instance, the nanoconfinement effects in homogeneous polymeric thin film systems were capable of inducing a 40 °C alternation from their bulk glass transition.[19]

Nanoparticle-filled polymeric systems also create nanoscale interfaces at the nanoparticle surface as well as a T_g shift.[20–23] Similarly to thin film geometry, polymer–particle interactions and particle sizes were critical factors affecting glass transition behavior in polymer nanocomposites. Attractive polymer–particle interactions led to an increase in T_g while repulsive interactions resulted in T_g reductions in homopolymers.[3] For favorable polymer–particle interaction systems, a T_g increase of 10 °C was reported for poly(methyl methacrylate) (PMMA) nanocomposites with 12 nm silica nanoparticles.[24] The inclusion of larger silica nanoparticles (diameter d = 30 nm) only resulted in a *ca.* 4 °C T_g increase for the PMMA matrices.[25] The nanoconfinement effects disappeared in 200–350 nm silica particle-filled PMMA and insignificant T_g changes were measured.[26] When polymer–particle interactions were non-wetting, silica nanoparticles reduced the T_g of polystyrene (PS) matrices by *ca.* 20 °C with the formation of agglomerates, highlighting the importance of polymer–particle interactions on the dispersion and thermal properties of

[a]*Department of Materials Science and Engineering and Beckman Institute, University of Illinois at Urbana-Champaign, Urbana, IL 61801, USA*
[b]*Department of Materials Science and Engineering, University of Delaware, Newark, DE 19716, USA*
[c]*Department of Chemical and Biomolecular Engineering, University of Delaware, Newark, DE 19716, USA. E-mail: wie@mit.edu*
[d]*School of Chemical Engineering, Sungkyunkwan University (SKKU), Suwon 440-746, Republic of Korea. E-mail: phs0727@skku.edu*

†Electronic supplementary information (ESI) available: ^{1}H NMR spectra of sPS and thermal stability of sPS nanocomposites are provided. See DOI: 10.1039/c5nr01151e

‡These authors contributed equally to this paper.

§Present address: Department of Mechanical Engineering, Massachusetts Institute of Technology, 77 Massachusetts Avenue, Cambridge, MA 02139, USA.

polymer nanocomposites.[6] Meth *et al*. revealed that the modification of particle surface chemistry could tailor polymer–particle interactions using methyl and amine functionalized silica nanoparticles in PMMA.[27]

In this study, we modified the surface chemistry of silica nanoparticles through amine-functionalization in order to manipulate interaction with nanoparticles as well as the double glass transition properties of the polymer nanocomposites. In particular, we report a concurrent enhancement and reduction of the glass transition temperature by using a random copolymer, sulfonated polystyrene (sPS), for controlled nanoparticle clustering and polymer phase separation.

Experimental section

Materials

Polystyrene (PS, M_w = 451 kDa, PDI = 1.06, Scientific Polymer Products, Inc.), acetic anhydride (99.5%, Aldrich), sulfuric acid (H_2SO_4, 95.0%, Samchun), MT-ST Organosilicasol™ (colloidal silica, 10–15 nm by BET method (Brunauer, Emmett and Teller), 30 wt% suspension in methanol, pH = 2–4, Nissan Chemical Co.), Ludox®HSA (colloidal silica, 12 nm, 30 wt% suspension in H_2O, deionized, pH = 3.5–5, W. R. Grace & Co.) and (3-aminopropyl)triethoxysilane (APTES, ≥98.0%, Aldrich) were used as received.

Synthesis of sulfonated polystyrene (sPS)

Acetyl sulfate was prepared prior to the sulfonation of PS. 5.42 mL of acetic anhydride were diluted in 28.2 mL dichloromethane in a 3–5 °C ice bath. Then, 2 mL of H_2SO_4 were added portion-wise and stirred for 1 h while maintaining the temperature, resulting in 1 M of acetyl sulfate. 4 g of PS were dissolved with 200 mL of dichloromethane in a 500 mL three-neck flask equipped with a condenser and dropping funnel. The solution was stirred at 40 °C under a slow stream of nitrogen. As-prepared 1 M acetyl sulfate was immediately transferred and added to the polymer solution at 40 °C using a dropping funnel (see Scheme 1). Certain aliquots of the solution were periodically extracted and quenched into 10 mL of 1-propanol and precipitated in 500 mL of deionized water. The degree of sulfonation of PS was controlled by adjusting the sulfonation time, including 1, 2 and 3 h. Finally, the obtained powder was dried at 70 °C in a vacuum oven for 3 days. The ^{1}H nuclear magnetic resonance (NMR) spectra of the synthesized sPS were collected on a JNM-AL300 (JEOL) with a proton frequency of 300 MHz (Fig. S1†). Deuterated dimethyl sulfoxide (DMSO) was chosen as the solvent and tetramethylsilane (TMS) was used as the internal standard.

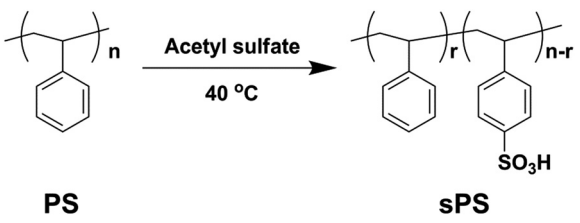

Scheme 1 Synthesis procedure of sulfonated polystyrene (sPS).

Surface functionalization of SiO_2 for amine-terminated SiO_2 (NH_2–SiO_2) nanoparticles

NH_2–SiO_2 nanoparticles were synthesized by functionalizing the surface of commercial grade SiO_2 nanoparticles readapting a protocol reported in previous literature.[28] 0.5 wt% of (3-aminopropyl) triethoxysilane (APTES) was added to 30 wt% of colloidal SiO_2 in deionized water. The mixture solutions were stirred overnight at room temperature and then isolated by centrifugation (10 000 rpm for 60 min) to remove the deionized water. The separated nanoparticles were washed with ethanol to remove the unreacted reagents and subsequently redispersed in methanol under sonication for 30 min.

Characterization of the nanoparticles

Visualization of the nanoparticles was achieved by transmission electron microscopy (TEM) using a JEM 2000FX (JEOL). TEM specimens were prepared by drop-casting the nanoparticle solutions in methanol onto carbon supported grids. The hydrodynamic diameters of SiO_2 and NH_2–SiO_2 were measured by a Zetasizer Nano ZS *via* dynamic light scattering (DLS) in methanol in dilute conditions. The zeta-potential measurement was conducted by a Brookhaven Instruments-PALS zeta potential analyzer.

Preparation of sPS nanocomposites

Sulfonated polystyrene was dissolved in methanol for 7 days, and SiO_2 and NH_2–SiO_2 nanoparticles were dispersed in methanol in a separated batch by applying sonication (Cole Parmer 8891) for 1 h. The 5 wt% and 20 wt% SiO_2 and NH_2–SiO_2 nanoparticles were mixed with the sPS solutions and further sonicated for 30 min. The mixtures were cast into a Teflon mold and free-standing sPS nanocomposite films were obtained through solvent evaporation for 7 days.

Characterization of sPS nanocomposites

FT-IR spectra of dried membranes and powder samples were recorded in the attenuated total reflectance (ATR) mode in the frequency range of 4000–650 cm^{-1} on a Nicolet 6700 instrument (Thermo Scientific, USA). The spectrum was recorded as the average of 32 scans with a resolution of 8 cm^{-1}. Each of the samples was put in equal physical contact with the sampling plate of the spectrometer accessory to avoid differences caused by pressure and penetration depth. The nanoparticles in the sPS matrix were visualized by a JEM 2000FX TEM. To prepare the TEM specimens, thin sections of the nanocomposites were microtomed and transferred onto copper grids. The dispersed states of the nanoparticles in the sPS matrix were also investigated by small angle X-ray scattering (SAXS) using an Ultima IV (Rigaku) with a wavelength of 1.542 Å at 44 kV–40 mA. The sample thicknesses were varied to achieve a transmission factor (ratio of the beam intensity after sample

insertion to the primary beam intensity without sample) range of 1/3 to 2/3 to ensure statistical credibility. The SAXS instrument was calibrated against a glassy carbon standard at the Advanced Photon Source (APS) and the obtained data were converted to absolute intensity by knowing the sample thickness and transmission factor. The thermal stability of the sPS nanocomposites was studied by thermal gravimetric analysis (TG) using a Q500 (TA instruments) with a ramp rate of 10 °C min^{-1} under nitrogen conditions. The glass transition temperature of the sPS nanocomposites was measured by differential scanning calorimetry (DSC) using a Discovery calorimeter (TA Instruments) in temperature-modulated mode under a nitrogen atmosphere. Temperature-modulated DSC (TMDSC) was calibrated with sapphire and the measurements were carried out with a temperature ramp rate of 5 °C min^{-1}, oscillation frequency period of 60 s and 1 °C amplitude followed by 5 min of isothermal process. The glass transition temperature (T_g) was obtained from the inflection point of the heat capacity from the reversible TMDSC thermograms.

Results and discussion

The focus of this work is the generation of double glass transition in polymer nanocomposites by the inclusion of surface-chemistry tailored nanoparticles. Amphiphilic sPS was used as the polymer matrix while silica (SiO_2) and amine-functionalized silica (NH_2–SiO_2) nanoparticles were used as fillers. The sPS was synthesized by sulfonating PS with acetyl sulfate. A sulfonation reaction for 1, 2 and 3 h was carried out at 40 °C and the sulfonation of the benzene ring was proportional with the time. The H^1-NMR spectra (see the ESI†) of sPS show that the sulfonation of the phenyl ring occurs at the *para*-position.[29] The signals at δ = 6.0–7.5 ppm from the phenyl rings of PS and sPS were clearly observed and assigned. The signals of non-sulfonated PS appeared at δ = 7.2–6.9 ppm (peak b) and δ = 6.8–6.0 (peak c).[30] As the sulfonation time increased, the new signal at δ = 7.5–7.2 ppm (peak a) gradually increased and was attributed to deshielding by the presence of neighboring *para*-substituted sulfonic acid groups attached to PS.[30] The degree of sulfonation (DS) of PS was calculated from the integral ratio of the proton peaks for sPS (I_a) and PS (I_b) in the ^{1}H NMR spectra as follows:

$$\mathrm{DS}\ (\%) = \{(I_a/2)/[(I_a/2) + (I_b/3)]\} \times 100, \quad (1)$$

where I_a and I_b indicate the integrals of the a and b proton peaks, respectively (Fig. S1†). Upon sulfonation, the DS values increased and were 18.5, 26.2, and 37.6% for 1, 2, and 3 h of sulfonation, respectively. The solubility of sPS was tested in different solvents as shown in Table S1.† For the sPS nanocomposites, sPS prepared with 3 h of sulfonation (DS = 37.6%) was utilized as the polymer matrix and methanol was chosen as the solvent.

The geometry and dimension of the nanoparticles were characterized by TEM and DLS. As shown in Fig. 1a and 1b, the nanoparticles were visualized by TEM and their spherical shapes were observed for both nanoparticles. The number-averaged hydrodynamic diameter (d_h) of SiO_2 nanoparticles was measured by DLS to be 13.5 ± 3.8 nm with a polydispersity index (PDI, the square of the standard deviation/mean diameter) of 0.08. Similarly, NH_2–SiO_2 nanoparticles had d_h = 14.5 ± 3.3 nm with PDI = 0.05. Considering PDI values smaller than 0.1, both nanoparticles could be monodispersed. The *z*-averaged diameter (d_z) of these monodispersed (PDI < 0.1) nanoparticles was calculated using the equation below and is summarized in Table 1,

$$d_z = <d> \frac{[z+3][z+2]}{[z+1]^2}, \quad (2)$$

where <*d*> is the number-averaged diameter and the value of *z* is given by $(1 - s^2)/s^2$, and *s* is the standard deviation/mean diameter. From the d_h and PDI information, the *z*-averaged

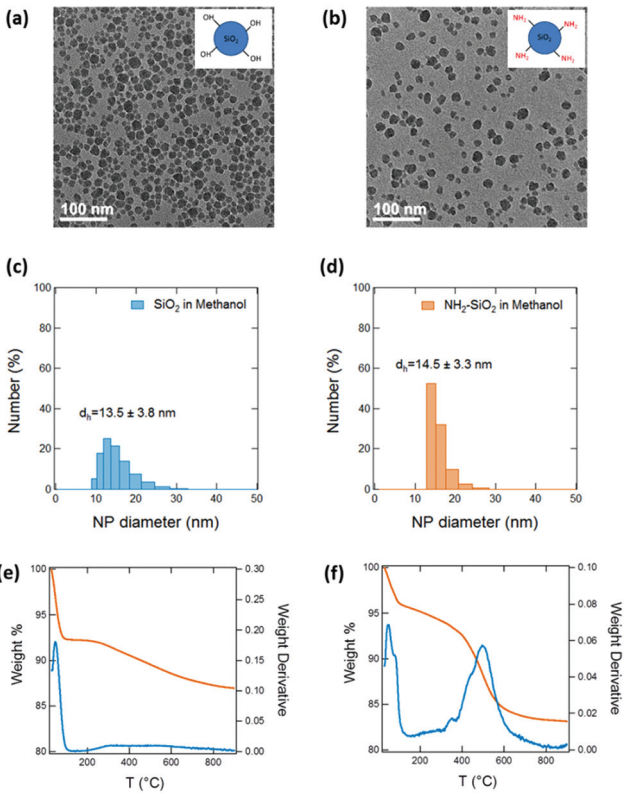

Fig. 1 TEM micrographs of (a) SiO_2 nanoparticles and (b) NH_2–SiO_2 nanoparticles. Histograms of the hydrodynamic diameter for (c) SiO_2 nanoparticles in methanol and (d) NH_2–SiO_2 nanoparticles in methanol. TGA thermograms for (e) SiO_2 nanoparticles and (f) NH_2–SiO_2 nanoparticles.

Table 1 Size information of the nanoparticles determined by DLS

	d_h (nm)	PDI	*z*	d_z (nm)
SiO_2	13.5 ± 3.8	0.08	11.6	16.9 ± 4.8
NH_2–SiO_2	14.5 ± 3.3	0.05	18.3	16.8 ± 3.8

diameter of SiO_2 was calculated to be 16.9 ± 4.8 nm, while d_z = 16.8 ± 3.8 nm was measured for NH_2–SiO_2 nanoparticles.

In addition to the geometry and dimension, the thermal stability of the nanoparticles was studied, as shown in Fig. 1e and 1f. The weight loss of SiO_2 nanoparticles below 100 °C was attributed to the water adsorbed onto hygroscopic sPS.[31] Oxide groups were decomposed above 100 °C and an inorganic residue corresponding to the silicon content was degraded at 900 °C. The amine moiety of NH_2–SiO_2 nanoparticles obviously caused different thermal decomposition patterns from SiO_2 nanoparticles, even though both of them contained nearly the same inorganic contents. The physisorbed water content decreased below 100 °C and the decomposition of the amine moiety appeared around 500 °C.[32]

Based on the TEM, DLS and TGA results, the amine-functionalization of silica nanoparticles was successfully achieved while the geometry and size remained constant.

Prior to preparing the polymer nanocomposites, the dispersion stability of the nanoparticles in methanol was investigated. Nanoparticles often aggregate due to their particle–particle attractive forces (*i.e.* van der Waals forces) and small interparticle gap. The nanoparticles can acquire thermodynamic stability against flocculation by employing steric and/or electrostatic repulsive forces that exceed particle–particle attractive forces.[33] In the example of steric stabilization, oleic acid ($C_{18}H_{34}O_2$) coatings on iron oxide nanoparticles provided steric repulsions due to its long alkyl chains.[34] In this study, however, the alkyl chains of the SiO_2 and NH_2–SiO_2 nanoparticles are not sufficiently long to provide steric repulsions, ruling out a steric stabilization mechanism. Hence, electrostatic repulsive forces are necessary to counterbalance the attractive forces.[35] Electrostatic repulsions can be introduced by charge stabilization, resulting in a Coulombic mutual repulsion of the electric double layers. A zeta potential of ±30 mV is often considered the threshold value for particle stability.[36] As shown in Table 2, time-resolved zeta potential measurements were carried out over the course of 24 h at ambient conditions in methanol. The zeta potential values after 24 h were measured to be −49.3 ± 1.4 mV and −44.6 ± 1.6 mV for SiO_2 and NH_2–SiO_2 nanoparticles, respectively, revealing their charge stabilized nature and thermodynamic stability.[37,38]

The sPS-nanoparticle composite films were prepared *via* solvent evaporation as described in the experimental section. The sPS-nanoparticle solutions were cast into a Teflon mold and free-standing sPS nanocomposite films were obtained after evaporating the solvent. Characteristic infrared absorbance peaks of the sulfonic groups in sPS are shown in Fig. 2: out-of-plane deformation bands from the sulfonic groups bonded to the polystyrene aromatic ring at 830–850 cm^{-1},[39] the symmetric stretching vibration of sulfonic groups at 1040 cm^{-1} and the peak from the sulfonate anion attached to a phenyl ring at 1127 cm^{-1}.[40] In particular, the sulfonate anion peak of neat sPS was red shifted by the inclusion of the nanoparticles, indicating favorable polymer–particle interactions.

Table 2 Time-resolved zeta potential measurements for nanoparticles in methanol

Time (h)	Zeta potential (mV), SiO_2 nanoparticles	Zeta potential (mV), NH_2–SiO_2 nanoparticles
0.1	−46.84 ± 1.38	−44.00 ± 0.48
1.0	−45.35 ± 1.98	−45.48 ± 1.09
2.0	−45.93 ± 1.83	−43.61 ± 2.01
24.0	−49.29 ± 1.39	−44.61 ± 1.56

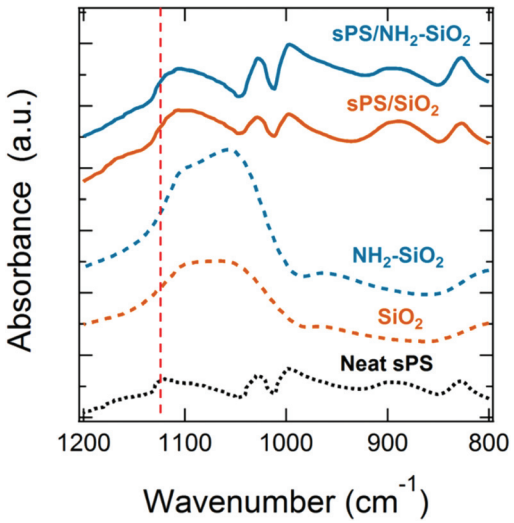

Fig. 2 FT-IR ATR spectra of neat sPS, SiO_2 and NH_2–SiO_2 nanoparticles, and sPS–SiO_2 and sPS–NH2–SiO_2 nanocomposites at 5 wt% filler loading.

Dispersion states of nanoparticles in sPS matrices were visualized by TEM images, as shown in Fig. 3. At 5 wt% loading, a nanoscale dispersion of SiO_2 was observed suggesting nanometric interparticle gaps. By assuming random particle packing, the interparticle distance can be estimated as below:[41]

$$\frac{H}{d} = \left(\frac{\phi_{max}}{\phi_{NP}}\right)^{1/3} - 1, \quad (3)$$

where H is the interparticle distance, d is the nanoparticle diameter, ϕ_{max} is the maximum volume fraction of 0.638 for random packing and ϕ_{NP} is the nanoparticle volume fraction. This equation estimates an interparticle distance of *ca.* 30 nm for 5 wt% SiO_2 nanoparticles, which is consistent with the results from the TEM micrographs. Although NH_2–SiO_2 nanoparticles are expected to have a similar interparticle distance at the same nanoparticle concentration, the interparticle distances were in the order of hundreds of nanometers, demonstrating a larger degree of agglomeration. Despite the agglomeration and high loading of NH_2–SiO_2 nanoparticles, a percolated structure by macro phase separation was not observed. At a higher concentration, 20 wt%, the interparticle distance of the SiO_2 nanoparticles was not discernible due to crowded nanoparticles. Notably, NH_2–SiO_2 nanoparticles had sub-micron clustering but no macroscopic phase separation occurred even at a 20 wt% filler loading.

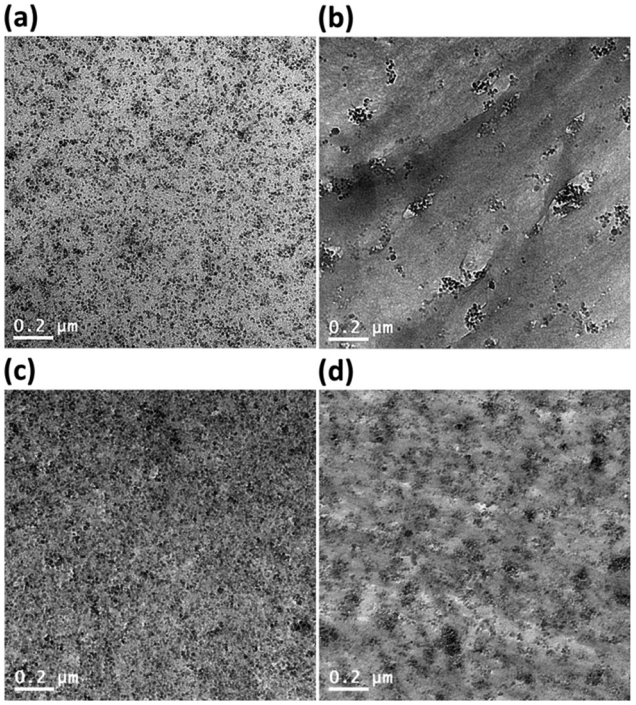

Fig. 3 TEM micrographs of sPS nanocomposite films: (a) sPS/5 wt% SiO_2, (b) sPS/5 wt% NH_2–SiO_2, (c) sPS/20 wt% SiO_2 and (d) sPS/20 wt% NH_2–SiO_2.

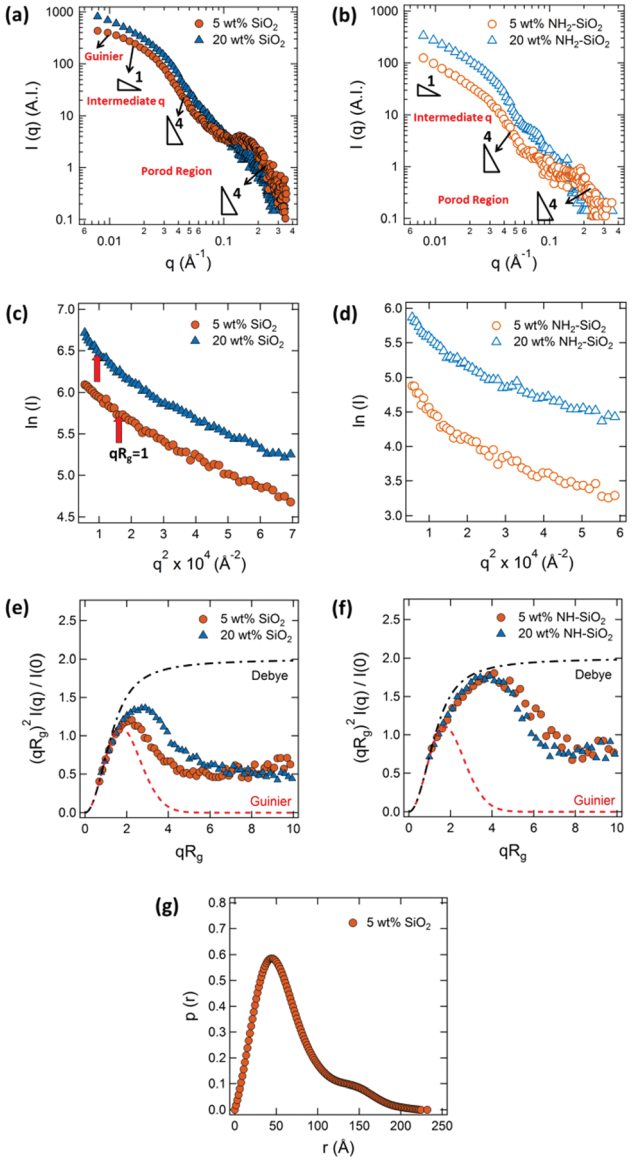

Fig. 4 SAXS intensity profiles *versus* q for (a) sPS–SiO_2 nanocomposites and (b) sPS–NH_2–SiO_2 nanocomposites. Guinier plots for (c) sPS–SiO_2 nanocomposites and (d) sPS–NH_2–SiO_2 nanocomposites. Normalized Kratky plot for (e) sPS–SiO_2 nanocomposites and (f) sPS–NH_2–SiO_2 nanocomposites. (g) Pair distance distribution function of sPS/5 wt% SiO_2 nanocomposites.

The microstructure of the sPS nanocomposites were further studied by the SAXS technique after which the collected data were calibrated against a glassy carbon standard from the APS to obtain absolute scattering intensity profiles. Fig. 4a and 4b illustrate the absolute intensity profiles of the sPS nanocomposites against a scattering vector, q. Qualitatively, the scattering intensity plateaus at low q ($qR_g < 1$); the Guinier region was achieved only with the 5 wt% SiO_2 nanoparticle system. The absence of intensity plateau regions at low q for the other systems indicates the formation of large agglomerates. Also, the absolute scattering intensity of the SiO_2 nanoparticle systems at a low wave vector (q) was much larger than that of the NH_2–SiO_2 nanoparticles despite having similar nanoparticle size, concentration and scattering length density. This finding was attributed to the larger length scale of the NH_2–SiO_2 nanoparticle agglomerates exceeding the measurement limits at the lowest q probed in this study. The Guinier region was followed by an intermediate q region with a power law of 1, a rod-like fractal dimension. Based on this rod-like fractal behavior, the agglomeration of several spherical particles can be expected. This will be discussed in more detail with the pair distance distribution function. After the intermediate region, the spherical conformation of the nanoparticles resulted in a scaling exponent of 4 in the Porod region, originating from the smooth surface of 3 dimensional objects. The scattering from q = 0.1 to 0.3 $Å^{-1}$ is attributed to the smeared oscillation of the particle form factor caused by polydispersity.[42] This modulation is observed only from the 5 wt% SiO_2 nanoparticles since agglomeration in other systems generates large structure factors. In the case of NH_2–SiO_2 nanoparticles, the Guinier region was not approached and the oscillation of the scattering profile was suppressed.

The quantification of the particle agglomerates was achieved through the Guinier equation below,

$$\ln I(q) = \ln I(0) - \frac{q^2 {R_g}^2}{3}, \quad (4)$$

where $I(0)$ is the scattering intensity extrapolated to zero q and R_g is the radius of gyration. The Guinier equation is an

approximate form which is valid only at the limit of $qR_g < 1$ (Guinier region) and only the 5 wt% SiO_2 nanoparticles satisfy this requirement at the lowest q probed in this study. The Guinier analysis generates the z-averaged R_g for the Gaussian coil and the d_z for compactly structured hard sphere can be obtained from $d_z = 2\sqrt{5/3}R_g$. The d_z of 5 wt% SiO_2 nanoparticle was calculated at the Guinier region to be 26.1 ± 4.6 nm. The z-averaged diameter of the SiO_2 nanoparticles dispersed in sPS was greater than that in methanol (d_z = 16.9 ± 4.8 nm), indicating that some agglomeration due to charge-neutralization during solvent evaporation occurred.[25] The linear slope of the 5 wt% SiO_2 nanoparticles (filled circles in Fig. 4c) in the Guinier plot strongly supports no further agglomerations, in contrast to the non-linear slopes for other nanoparticle systems due to their larger scale clustering behavior.

The conformation of nanoparticles is investigated by the normalized dimensionless Kratky plot as shown in Fig. 4e and 4f. The Kratky plot is based on approximated form factor equations in the high q limit ($q > 5/R_g$),[43] providing internal structure information. A Gaussian chain or asymmetric particles are expected to have an asymptotic plateau in the high q region due to their asymptotic behavior in q^{-2}, as given by Debye's law:

$$\frac{I(q)}{I(0)} = \frac{2(x - 1 + \exp(-x))}{x^2}, \quad (5)$$

where $x = (qR_g)^2$.

Meanwhile, spherical particles display bell-shaped curves as they show asymptotic behavior in q^{-4}, following Guinier's law as shown in eqn (4). Due to the relationship in the Guinier plot, the $(qR_g)^2\ I(q)/I(0)$ value in the dimensionless Kratky plot is 1.104 at $qR_g = \sqrt{3}$. Clearly, all the particle systems followed bell-shaped curves with the expected y-axis value at $qR_g = \sqrt{3}$. However, the qR_g value at maximum $(qR_g)^2\ I(q)/I(0)$ shifted to a higher qR_g region when compared to the ideal spherical case. It indicates that clustering of nanoparticles increased aspect ratio of the feature and form factor deviate from the ideal symmetric particle geometry. In comparing the 5 wt% and 20 wt% SiO_2 nanoparticle cases, larger deviations along both the x- and y-axes were found from the 20 wt% SiO_2 nanoparticle's Kratky plot due to larger clustering with higher particle concentration. This deviation becomes more pronounced in NH_2–SiO_2 nanoparticle systems while similar concentration dependent results are observed. The peak qR_g value increased to 4 and the peak $(qR_g)^2\ I(q)/I(0)$ value reached 1.8.

To further quantify the geometry, the pair distance distribution function (PDDF, $p(r)$) was introduced for 5 wt% SiO_2 nanoparticles where the least clustering occurred in this study. The $p(r)$ value calculated from direct integration suffers from severe distortion by the q truncation. Hence, the indirect Fourier transform is employed by GNOM as below,

$$I(q) = 4\pi \int_0^\infty p(r) \frac{\sin(qr)}{qr} \mathrm{d}r \quad (6)$$

As is apparent in Fig. 4g, most nanoparticles are dispersed as individual particles while a small portion of particles displayed clustering. Overall, the SAXS results agreed well with the dispersion states of the nanoparticles visualized by the TEM micrographs.

The glass transition and polymer relaxation of sPS nanocomposites were characterized from the reversing heat flow data as measured through the TMDSC technique. TMDSC superimposes a small temperature modulation onto a linear heating rate of conventional DSC. This temperature modulation enables the deconvolution of reversible and non-reversible components from the total heat flow. Hence, a reversible heat flow excludes signals originating from kinectic-related enthalpic relaxation and true heat capacity can be obtained for the rigid amorphous fraction.

In sPS nanocomposites, the presence of nanoparticles dispersed at the nanoscale restrict polymer segmental mobility due to steric effects, reducing polymer chain interdiffusion or relaxation.[44–47] Indeed, the SiO_2 nanoparticle systems revealed a depression in the magnitudes of heat flow changes around T_g compared to neat sPS, which is indicative of a reduced polymer chain relaxation, as shown in Fig. 5a. At the 20 wt% particle loading, enhanced steric effects further suppressed chain relaxation compared to the 5 wt% concentration. While the agglomeration of 5 wt% NH_2–SiO_2 nanoparticles decreased the steric effects and the restricted polymer relaxation behavior was not observed, the 20 wt% NH_2–SiO_2 nanoparticles were capable of generating steric effects again by the reduced interparticle distance.

In addition to restricting polymer segmental mobility, nanoscale-dispersed nanoparticles can increase the T_g of the polymer matrix. In SiO_2 nanoparticle systems, the T_g increased by approximately 10 °C with the inclusion of nanoparticles. Remarkably, the surface chemical modification of the SiO_2 nanoparticles by amine moieties resulted in revealing two distinct glass transitions of the sPS nanocomposites, suggesting a phase separation of sPS. Although two T_g behaviors have often been found from micro phase separated di-block copolymers, the nanoparticle-induced double T_g phenomenon in a random copolymer (PS-*co*-sPS) has yet to be explored, distinguishing this work from others.

Along with the aforementioned structure–property relations, polymer–particle interactions are also a significant parameter for the polymer T_g. Favorable polymer–particle interactions can create locally stiffened polymer layers due to the adsorption of polymer onto the nanoparticle surfaces, which increases the effective polymer T_g.[44] This immobilized interfacial layer around the nanoparticle surfaces is referred to as the rigid amorphous fraction (RAF).[48,49] Nanocomposites without RAF contain no strong polymer–particle attractive forces and are not expected to acquire a significant T_g increase. Meth *et al*. reported only an increase of *ca*. 2 °C for the T_g in the PS nanocomposites at 10 vol% of silica nanoparticle ($d \sim$ 30 nm) loading, and so RAF was not observed in their systems.[25] After accounting for density differences, similar concentrations were compared and found to have 7.3 and 9.3 °C increases of T_g from the 20 wt% SiO_2 and 20 wt% NH_2–SiO_2 nanocomposites, respectively. The T_g increase of the

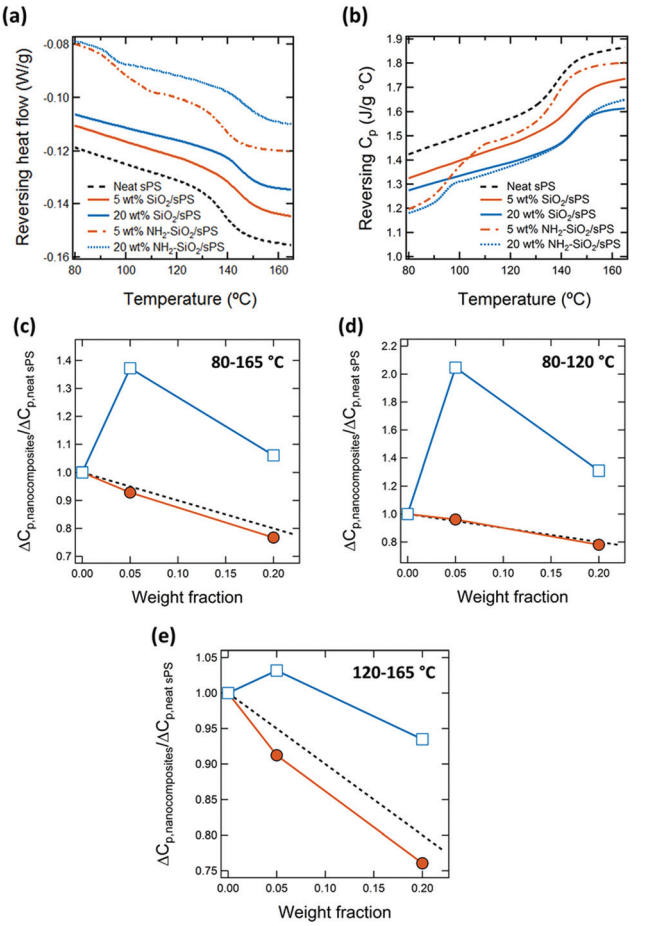

Fig. 5 Thermal properties of sPS nanocomposites. (a) Reversing heat flow profiles measured by TMDSC, (b) reversing heat capacity profiles near T_g and plots of $\Delta C_{p(nanocomposites)}/\Delta C_{p(sPS)}$ *versus* nanoparticle weight fraction in the temperature ranges of (c) 80 °C to 165 °C, (d) 80 °C to 120 °C and (e) 120 °C to 165 °C for neat sPS and sPS–SiO_2 and sPS–NH_2–SiO_2 nanocomposites. The black dashed lines are the prediction for composites without a rigid amorphous fraction. The dashed lines (---), filled circles (●) and unfilled rectangles (□) in (c)–(e) are the predictions without RAF, $\Delta C_{p(nanocomposites)}/\Delta C_{p(sPS)}$ for the sPS–SiO_2 nanocomposites and $\Delta C_{p(nanocomposites)}/\Delta C_{p(sPS)}$ for the sPS–NH_2–SiO_2 nanocomposites, respectively.

NH_2–SiO_2 nanocomposites was greater than that of SiO_2 nanocomposites, showing a stronger polymer–filler interaction in the NH_2–SiO_2 nanoparticle system. In regards to the weak interactions between PS and the SiO_2 nanoparticles, the formation of RAF was derived from the favorable interaction between sPS and the nanoparticles. In order to further elucidate the correlation of the T_g increase with the nanoconfinement effects, RAF was calculated from the heat capacity, C_p, information presented in Fig. 5b using the equation below,

$$\text{RAF} = 1 - \text{filler content} - \Delta C_p, \text{composites}/\Delta C_p, \text{polymer} \quad (7)$$

where a difference in C_p values between the glassy and rubbery states (ΔC_p) of the composites is ΔC_p,composites and ΔC_p of neat polymer is ΔC_p,polymer. Positive RAF value indicates the formation of RAF.

The normalized C_p values of the sPS nanocomposites are shown in Fig. 5c and deconvoluted into 80–120 °C and 120–165 °C temperature ranges in Fig. 5d and 5e, respectively. The normalized C_p values of the SiO_2 nanocomposites in the region of 80–120 °C are consistent with the predicted values by taking only the filler effects into account (black dashed line). Conversely, the normalized C_p values of the SiO_2 nanocomposites are smaller than that of the prediction in the region of 120–165 °C, suggesting the formation of RAF. The immobilized RAF is located in the proximity of 145 °C and 0.04 of RAF was calculated for both 5 wt% and 20 wt% SiO_2 nanocomposites. The formation of RAF in the sPS–SiO_2 nanoparticle composites was attributed to the strong polymer–filler interactions. In contrast, negative RAF values were calculated for NH_2–SiO_2 nanoparticles in the entire temperature ranges: −1.10 for 5 wt% and −0.51 for 20 wt% in the 80–120 °C temperature range and −0.08 for 5 wt% and −0.13 for 20 wt% in the 120–165 °C temperature range. As the fraction cannot exceed unity, relaxation located in the proximity of 100 °C originated from a different mechanism, the nanoparticle-induced phase separation of the polystyrene domain (T_g = 105 °C). The plasticization (T_g = 97.3 and 93.2 °C for 5 wt% and 20 wt% NH_2–SiO_2 nanoparticle loading, respectively) of PS was associated with improved polymer segmental motions in concomitant with increased free volume in phase separated PS domain by the inclusion of nanoparticles. Previous literature also reported a similar glass transition depression, such as PS–SiO_2 (d = 15 nm) nanocomposites[6] and charge neutralized sPS *via* amine-chemistry based counterions,[50] but only a single T_g was observed in their systems. In this study, T_g reduction is not related to other chemical identities, such as organic solvents (methanol) and adsorbed water. Absence of additional T_g near this temperature range from the hydrophilic SiO_2 nanoparticle systems ruled out these possibilities.

Conclusions

In summary, we have demonstrated the double glass transition of sulfonated polystyrene matrices by the inclusion of nanoparticles and considered the structure–property relationships. sPS itself has only a single glass transition temperature and the nanoscale dispersion of charge stabilized 14 nm SiO_2 nanoparticles resulted in a T_g increase up to 7.3 °C in sPS. This T_g increase originated from the strong polymer–particle interactions, as evidenced by the presence of RAF as well as the steric nanoconfinement effect, restricting polymer segmental mobility. When the amine surface chemistry is employed onto silica nanoparticles, the sub-micron scale clustering is found in addition to nanoscale dispersion. With these two distinct nanoparticle dispersion states, a double glass transition phenomenon is observed, indicating a phase separation of the PS domains from sPS. The surface chemistry dependent structure–property relation of sPS-silica nanoparticle nanocompo-

sites would provide important insights for the design of polymer–nanoparticle nanocomposites, considering that sPS can be used as a proton exchange membrane and silica is a widely used filler in various industries, including rubbers, coatings, paints and plastics.

Acknowledgements

This work was supported by the Basic Science Research Program through the National Research Foundation (NRF) of Korea funded by the Ministry of Science, ICT & Future Planning (2012R1A1A2044094). We thank the W. M. Keck Electron Microscopy Facility at the University of Delaware. We also thank Prof. Michael Mackay (SAXS, DSC, and TGA), Prof. Norman Wagner (zeta-potential analyzer), Prof. Xinqiao Jia (DLS) and Advanced Materials Characterization Lab at the University of Delaware (ATR-FTIR) for access to the instruments.

Notes and references

1 Z. Yang, Y. Fujii, F. K. Lee, C.-H. Lam and O. K. C. Tsui, *Science*, 2010, **328**, 1676.
2 C. J. Ellison and J. M. Torkelson, *Nat. Mater.*, 2003, **2**, 695.
3 H. Oh and P. F. Green, *Nat. Mater.*, 2009, **8**, 139.
4 S. Chandran, J. K. Basu and M. K. Mukhopadhyay, *J. Chem. Phys.*, 2013, **138**, 014902.
5 S. Chandran and J. K. Basu, *Eur. Phys. J. E: Soft Matter Biol. Phys.*, 2011, **34**, 1.
6 A. Bansal, H. C. Yang, C. Z. Li, K. W. Cho, B. C. Benicewicz, S. K. Kumar and L. S. Schadler, *Nat. Mater.*, 2005, **4**, 693.
7 P. Rittigstein, R. D. Priestley, L. J. Broadbelt and J. M. Torkelson, *Nat. Mater.*, 2007, **6**, 278.
8 O. Baeumchen, J. D. McGraw, J. A. Forrest and K. Dalnoki-Veress, *Phys. Rev. Lett.*, 2012, 109.
9 M. K. Mundra, C. J. Ellison, R. E. Behling and J. M. Torkelson, *Polymer*, 2006, **47**, 7747.
10 C. H. Park, J. H. Kim, M. Ree, B. H. Sohn, J. C. Jung and W. C. Zin, *Polymer*, 2004, **45**, 4507.
11 L. R. Arriaga, F. Monroy and D. Langevin, *Europhys. Lett.*, 2012, 98.
12 C. Zhang, Y. Fujii and K. Tanaka, *ACS Macro Lett.*, 2012, **1**, 1317.
13 P. A. O'Connell, J. Wang, T. A. Ishola and G. B. McKenna, *Macromolecules*, 2012, **45**, 2453.
14 J. L. Keddie, R. A. L. Jones and R. A. Cory, *Europhys. Lett.*, 1994, **27**, 59.
15 J. L. Keddie, R. A. L. Jones and R. A. Cory, *Faraday Discuss.*, 1994, **98**, 219.
16 S. Napolitano and M. Wubbenhorst, *Nat. Commun.*, 2011, 2.
17 R. Inoue, K. Kawashima, K. Matsui, T. Kanaya, K. Nishida, G. Matsuba and M. Hino, *Phys. Rev. E: Stat. Phys., Plasmas, Fluids, Relat. Interdiscip. Top.*, 2011, 83.
18 R. Inoue, T. Kanaya, K. Nishida, I. Tsukushi, M. T. F. Telling, B. J. Gabrys, M. Tyagi, C. Soles and W. I. Wu, *Phys. Rev. E: Stat. Phys., Plasmas, Fluids, Relat. Interdiscip. Top.*, 2009, 80.
19 C. B. Roth, K. L. McNerny, W. F. Jager and J. M. Torkelson, *Macromolecules*, 2007, **40**, 2568.
20 A. Papon, H. Montes, M. Hanafi, F. Lequeux, L. Guy and K. Saalwaechter, *Phys. Rev. Lett.*, 2012, 108.
21 V. Arrighi, I. J. McEwen, H. Qian and M. B. S. Prieto, *Polymer*, 2003, **44**, 6259.
22 P. Rittigstein and J. M. Torkelson, *J. Polym. Sci., Part B: Polym. Phys.*, 2006, **44**, 2935.
23 F. D. Blum, E. N. Young, G. Smith and O. C. Sitton, *Langmuir*, 2006, **22**, 4741.
24 N. Garia, T. Corrales, J. Guzman and P. Tiemblo, *Polym. Degrad. Stab.*, 2007, **92**, 635.
25 J. S. Meth, S. G. Zane, C. Z. Chi, J. D. Londono, B. A. Wood, P. Cotts, M. Keating, W. Guise and S. Weigand, *Macromolecules*, 2011, **44**, 8301.
26 V. M. Boucher, D. Cangialosi, A. Alegria and J. Colmenero, *Macromolecules*, 2010, **43**, 7594.
27 M. Qu, J. S. Meth, G. S. Blackman, G. M. Cohen, K. G. Sharp and K. J. Van Vliet, *Soft Matter*, 2011, **7**, 8401.
28 W.-K. Oh, S. Kim, M. Choi, C. Kim, Y. S. Jeong, B.-R. Cho, J.-S. Hahn and J. Jang, *ACS Nano*, 2010, 4.
29 J. C. Yang, M. J. Jablonsky and J. W. Mays, *Polymer*, 2002, **43**, 5125.
30 M. J. Park, A. J. Nedoma, P. L. Geissler, N. P. Balsara, A. Jackson and D. Cookson, *Macromolecules*, 2008, **41**, 2271.
31 I. J. Dijs, H. L. F. van Ochten, A. J. M. van der Heijden, J. W. Geus and L. W. Jenneskens, *Appl. Catal., A*, 2003, **241**, 185.
32 A. Ōya, M. Saito and S. Ōtani, *Appl. Clay Sci.*, 1988, **3**, 291.
33 R. G. Larson, *The structure and rheology of the complex fluids*, Oxford, 1999.
34 R. Tadmor, R. E. Rosensweig, J. Frey and J. Klein, *Langmuir*, 2000, **16**, 9117.
35 R. P. Bagwe, L. R. Hilliard and W. Tan, *Langmuir*, 2006, **22**, 4357.
36 P. Sherman, *Industrial rheology*, Academic Press Inc., London, 1970.
37 J. Jiang, G. Oberdorster and P. Biswas, *J. Nanopart. Res.*, 2009, 11.
38 D. Hanaor, M. Michelazzi, C. Leonelli and C. C. Sorrell, *J. Eur. Ceram. Soc.*, 2012, 32.
39 F. Kucera, Ph.D. Thesis, Technical University of Brno, 2001.
40 R. A. Weiss, A. Sen, C. L. Willis and L. A. Pottick, *Polymer*, 1991, **32**, 1867.
41 M. E. Mackay, A. Tuteja, P. M. Duxbury, C. J. Hawker, B. Van Horn, Z. B. Guan, G. H. Chen and R. S. Krishnan, *Science*, 2006, **311**, 1740.
42 N. J. Fernandes, J. Akbarzadeh, H. Peterlik and E. P. Giannelis, *ACS Nano*, 2013, **7**, 1265.

43 S. Gagliardi, V. Arrighi, R. Ferguson, A. C. Dagger, J. A. Semlyen and J. S. Higgins, *J. Chem. Phys.*, 2005, 122.
44 M. Kobayashi, Y. Rharbi, L. Brauge, L. Cao and M. A. Winnik, *Macromolecules*, 2002, **35**, 7387.
45 J. Typek, N. Guskos, A. Szymczyk and D. Petridis, *J. Non-Cryst. Solids*, 2008, **354**, 4256.
46 S. Gam, J. S. Meth, S. G. Zane, C. Chi, B. A. Wood, K. I. Winey, N. Clarke and R. J. Composto, *Soft Matter*, 2012, **8**, 6512.
47 S. Gam, J. S. Meth, S. G. Zane, C. Chi, B. A. Wood, M. E. Seitz, K. I. Winey, N. Clarke and R. J. Composto, *Macromolecules*, 2011, **44**, 3494.
48 P. S. Thomas, S. Thomas, S. Bandyopadhyay, A. Wurm and C. Schick, *Compos. Sci. Technol.*, 2008, **68**, 3220.
49 A. Sargsyan, A. Tonoyan, S. Davtyan and C. Schick, *Eur. Polym. J.*, 2007, **43**, 3113.
50 R. A. Weiss, P. K. Agarwal and R. D. Lundberg, *J. Appl. Polym. Sci.*, 1984, **29**, 2719.